Estimation of Fukushima radio-cesium deposits by airborne surveys: sensitivity to the flight-line spacing

Pedram Masoudi, Mathieu Le Coz, Marc Andre Gonze, Charlotte Cazala

Estimation of Fukushima radio-cesium deposits by airborne surveys: sensitivity to the flight-line spacing

Pedram MASOUDI[1], Mathieu LE COZ[1], Marc-André GONZE[2], Charlotte CAZALA[1]

[1]Institut de Radioprotection et de Sûreté Nucléaire (IRSN), PSE-ENV/SEDRE, 31 avenue de la Division Leclerc, 92260 Fontenay-aux-Roses, France

[2]Institut de Radioprotection et de Sûreté Nucléaire (IRSN), PSE-ENV/SEREN, 13115 Saint-Paul-lez-Durance, France

Highlights:

- Geostatistical mapping of ^{137}Cs ground activity from airborne gamma-ray data
- Punctual and characterization errors as a function of flight-line spacing
- Sensitivity of the mapping to the spatial structure of the contamination

Abstract

After Fukushima Daiichi Nuclear Power Plant (FDNPP) accident, airborne gamma-ray detection was used for regional mapping of soil contamination. For such surveys, the flight-line spacing is an important factor controlling the quality of contamination maps. In this study, cesium-137 (^{137}Cs) ground activity is interpolated and mapped using ordinary kriging method; thereafter the error of interpolation is evaluated as a function of flight-line spacing. The analyses were conducted in six 20 km × 20 km test sites with distance of less than 80 km from the FDNPP. In each site, the ordinary kriging estimators were applied to different selections of flight-lines of decreasing density, then punctual and classification errors were calculated. It is demonstrated that these variables are highly correlated (r^2>0.78): increasing the flight-line spacing for 1 km increases the errors from 3% to 9%, depending on the site location. Therefore, flight-line spacing could be designed as a function of acceptable error, determined in the monitoring objectives.

Keywords: Geostatistical radiological mapping; flight-line spacing optimization; sampling design; nuclear accident and post-accidental monitoring.

1. Introduction

Following the major accident of the Fukushima Daiichi Nuclear Power Plant (FDNPP) in March 2011, large amounts of radionuclides were released and deposited onto the continental and oceanic surfaces (Saito and Onda, 2015). The soil gamma-ray measurements performed in July 2011 showed that more than 99% of the air dose rate originated from radio-cesium isotopes (Saito et al., 2015). In order to assess the temporal evolution of radio-cesium ground activity in contaminated territories of the Fukushima region (i.e., up to ~80 km from the FDNPP), airborne gamma-ray surveys were performed periodically since the accident (Sanada et al., 2014; Le Coz et al., 2019). The airborne sampling design varies from a survey to another; e.g., between 2011 and 2013, the spacing between flight-lines ranged from 600 m to 2 km depending on the survey (JAEA, 2014).

Airborne geophysical surveys are commonly used to investigate physical properties of the earth over a large region (e.g., Airo et al., 2011; Kass, 2013). The design of an airborne survey consists of determining flight-line direction and spacing, in addition to determining flight height and speed (Minty, 1997; Kass, 2013). Almost always, the acquired data is denser along the flight-lines than perpendicular to them. Hence, the flight-lines are designed parallel to the direction of maximum variability (if it exists and is known), and the flight-line spacing should be as dense as not to miss local hot-spots between lines, i.e., aliasing (Reeves, 2005). The flight-line spacing is recommended to be one kilometer or greater, for a regional or national scale inventory investigation; and between 50 m and 400 m is suggested for detailed mapping. In particular cases, e.g., individual field boundaries and search for radioactive sources, flight-line spacing could be designed to be 50 m or even less (IAEA, 2003).

In case of nuclear accidents, where there is long-distance propagation of radionuclides through the environment, airborne gamma-ray measurement is considered to be completely relevant for post-

accident reconnaissance (Sanderson et al., 2001). The effect of flight-line spacing on the estimation of ^{137}Cs inventory in ground was assessed in three areas of NW England and SW Scotland (Sanderson et al., 2008): the increase in flight-line spacing (subsampling), from 50 to 500 m (10 km × 10 km area) and from 500 m to 5 km (50 km × 50 km area), was shown to preserve the general outline of depositional area, and the difference in the estimated inventories was below 10%; however, local variations were not clearly defined by the sparser surveys. In fact, flight-line spacing should be designed in order to obtain an optimal trade-off between the survey costs (financial, time delay, sampling limitations, etc.) and its objectives (level of contamination, waste volume, desired resolution, etc.), which is different for every situation (Desnoyers and Dubot, 2014a, b).

This study aims at investigating and quantifying the effect of flight-line spacing on interpolation of the ^{137}Cs ground activity from airborne gamma-ray spectrometry survey in the Fukushima region. To this end, ^{137}Cs maps are generated based on subsets of measurements acquired during a relatively dense airborne survey for six 20 km × 20 km sites located within the FDNPP 80 km zone. Both punctual and classification errors are then computed from the maps obtained with various subsets.

2. Data and method

2.1. Datasets

After Fukushima accident, a series of gamma-ray airborne surveys were conducted by the Ministry of Education, Culture, Sports, Science and Technology (MEXT) on a semi-circle region with 80 km radius centered at the FDNPP (Fig. 1a). The counting rate at the flying altitude was converted into a deposit estimated at ground surface by applying the following transformations: (i) altitude correction to 1 m a.g.l.; (ii) conversion of count rates to dose rates; and (iii) conversion of dose rates into ground activity of ^{137}Cs (in Bq.m^{-2}) (Gonze et al., 2014). The processed data and further descriptions are publicly available (JAEA, 2014).

The airborne measurement and the derived parameters are generally attributed to a circular area on the ground, beneath the detector, called Field of View (FOV). For the Fukushima surveys, the radius of FOV is recommended to be considered equal to the detector height, namely about 350 m (Lyons and Colton, 2012). At this height, more than 75% of recorded gamma-ray is originated from the FOV (Malins et al., 2015). In addition, since airborne measurement is performed along the flight-lines, the sampling spacing is minimum parallel to the flight-lines, about 40 m depending on the flight speed. Perpendicular to the flight-lines, the sampling spacing is significantly higher, in the order of several hundred meters, and depends on both the survey and the location (Tables 1 and 2).

For investigating mapping sensitivity to flight-line spacing, the 8th airborne survey (airborne #8, November 2013), which is the densest available airborne survey, was selected. The study focuses on six square 20 km × 20 km test sites (T1 to T6 on Fig. 1a and Table 2) representing a variety of geographical and land-use situations as well as a wide range of ^{137}Cs ground activity (Fig. 2). In each test site, a unique set of points (91 to 136 depending on the density of data) was kept out from the original dataset for validation purpose (Fig. 1b). Then, a series of datasets was generated by removing flight-lines (i.e., sub-sampling) in order to increase the sampling distance between flight-lines (Table 3).

2.2. Interpolation procedure

In each test site, ^{137}Cs was interpolated using each flight-line selection. The interpolation procedure, based on the geostatistical theory of kriging, was carried out by means of Isatis commercial software (Bleines et al., 2004):

i. Since the distribution of ^{137}Cs is often lognormal, it was transformed to logarithmic scale.

ii. Geostatistical methods are basically developed for interpolating stationary data (Chiles and Delfiner, 2012); previous analyses of Fukushima airborne data yet showed that variability in log(^{137}Cs) is generally nonstationary in distance of 20 km (Masoudi et al., 2019). Since

experimental semi-variogram is not conformable, a trend (deterministic model) was thus fitted by moving average (Table 4) and removed from log(^{137}Cs), resulting in residual.

iii. The distribution of residual was transformed to the normal Gaussian distribution through the frequency inversion anamorphosis algorithm (Bleines et al., 2004).

iv. The experimental semi-variogram of residual was computed and a spherical model was fitted. For various distances between pairs of points, the semi-variogram describes the half mean of square difference in residual (Chiles and Delfiner, 2012).

v. Point ordinary kriging was applied to estimate the residual at the location of validation points (Fig. 1b). This kriging system considers that mean of data around the estimation point is constant but unknown (Wackernagel, 2003).

vi. The punctual estimations were back transformed to the pre-anamorphosis distribution, summed with the deterministic model and back transformed to the scale of initial data, in order to be comparable with ^{137}Cs values at validation points.

vii. Ordinary block kriging was applied to estimate the average residual on square grid cells with 250 m sides covering whole the area of test site. Indeed, the block kriging system is an adaptation of point kriging for continuous data within surface or volume (Wackernagel, 2003).

viii. The estimated values were back transformed to the pre-anamaprhosis distribution, summed with the deterministic model and back transformed to the scale of initial data, in order to produce ^{137}Cs contamination map.

The kriging interpolation procedure not only provides an estimated value but also variance of estimation error, a measure of estimation uncertainty (Journel et al., 2000). Kriging estimations and variances were used in turning bands simulation in order to generate 100 possible realizations of the ^{137}Cs map (Chiles and Delfiner, 2012). The simulation was done for each flight-line selection on test site T1.

121 *2.3. Interpolation errors*

122 The punctual error was computed by comparing ^{137}Cs values estimated at the validation points
123 through point ordinary kriging by considering each flight-line selection and all flight lines:

124 $$E_p = \frac{1}{n}\sum_{i=1}^{n}\frac{\left|v_i^{sel} - v_i^{all}\right|}{v_i^{all}} \quad \text{[Eq. 1]}$$

125 were E_p is the punctual error; n is the number of validation points; v_i^{sel} and v_i^{all} are estimated ^{137}Cs
126 ground activity (kBq.m^{-2}) at point i using a selection of flight-lines and all flight-lines, respectively.

127 The ^{137}Cs contamination maps produced by ordinary block kriging interpolation were used to classify
128 each test site to contaminated and not contaminated areas, given a contamination threshold.
129 Overlapping real and estimated contamination areas partitions each test site to four surfaces (Fig. 3),
130 and a classification error is computed as the ratio of misclassified surfaces to the real contamination
131 area:

132 $$E_c = \frac{S2+S3}{S1+S2} \quad \text{[Eq. 2]}$$

133 where E_c is the classification error; $S1$ is correctly characterized contaminated surface; $S2$ and $S3$ are
134 false negative and false positive characterized surfaces, respectively. In practice, the real
135 contaminated area is unknown, however the contamination map, produced using all the flight-lines,
136 resembles to the reality the most. Hence, this map is considered as the reference for calculating the
137 classification error of other flight-line selections. This error is calculated as a function of
138 contamination threshold.

139 In the interpolation procedure (Sect.2.2), the flight-line spacing influences the variography analysis
140 (stage iv) and controls the neighboring data configuration of kriging estimators (stages v and vii). In
141 order to measure the sensitivity of results to variogram model, interpolation procedure was repeated
142 in test site T1 for all the selections, using the fixed variogram computed using all flight-lines. Both the

143 punctual and classification errors were then computed and compared to the errors computed by
144 updated models.

145 2.4. Kriging uncertainty

146 In test site T1, the influence of increasing flight-line spacing on the kriging uncertainty was
147 investigated based on the sets of 100 realizations generated by turning bands simulation. More
148 precisely, the relation between the flight-line spacing and the average of standard deviations of the
149 simulated ^{137}Cs values (i.e., on the 100 realizations) at each validation point were analyzed. In
150 addition, the relation between the flight-line spacing and standard deviation of the misclassified area
151 computed based on the 100 realizations for a given threshold was analyzed.

152 **3. Results**

153 *3.1. Experimental semi-variograms*

154 The experimental semi-variograms computed orthogonal to the flight-lines (Fig. 4) shows that spatial
155 correlation of ^{137}Cs is the shortest for test site T2, lower than 5 km. In this test site, the increase of
156 flight-line spacing clearly impacts the quality of the experimental semi-variogram: in 1/3 sub-
157 sampling, the flight-line spacing becomes larger than spatial correlation (Fig. 4b). The experimental
158 semi-variograms computed for test site T4 also show a relatively short spatial correlation, about 5
159 km, which cannot be identified from the scarcer sub-sampling (Fig. 4d). For the other test sites, the
160 experimental semi-variograms show similar behavior whatever the sub-sampling, particularly for the
161 test site T3, for which the spatial correlation is the longest, farther than 15 km (Fig. 4c).

162 *3.2. Punctual and classification errors*

163 In test site T1, the cross-plot of punctual error versus flight-line spacing shows a high positive
164 correlation (r^2=0.86, Fig. 5). This relationship was modeled by fitting a linear regression, revealing
165 that increase of one kilometer in flight-line spacing results in 4% increase in the punctual error, with

166 an uncertainty range of less than ±1% for shortest flight-line spacing up to ±5% for 5 km flight-line
167 spacing. The punctual errors computed in test sites T2 to T5 are compatible with the linear regression
168 model established for T1. However, the punctual error increases more rapidly in T6, i.e., 8% increase
169 in error for 1 km increase in flight-line spacing (Fig. 5).

170 In test site T1, increasing the flight-line spacing from 1.3 to 4.0 km increases the classification error
171 two to three times whatever the threshold value (the classification error is yet more marked for high
172 threshold values, i.e., a small contaminated areas) (Fig. 6). Particularly, at threshold P75, i.e. the third
173 quartile (Table 2), of the same test site, there is a strong linear correlation (r^2=0.79) between the
174 classification error and flight-line spacing (Fig. 6). This relationship was fitted by a linear regression
175 model showing that the increase of one kilometer in the flight-line spacing increases the classification
176 error by 5%. The dispersion pattern of the points around the regression line shows lower uncertainty
177 (±5%) in small flight-line spacing than in large flight-line spacing (±10%) (Fig. 7). The classification
178 error values computed in test sites T4, T5 and T6 are compatible with the linear regression model
179 established in T1; but estimations in T2 and T3 tend to maximize and minimize the classification
180 error, respectively.

181 For test site T1, using a fixed variogram model results in nearly the same punctual errors as updated
182 variogram (Fig. 8a), illustrating that the punctual error is not significantly sensitive to the accuracy of
183 variogram model. By contrast, the fixed variogram model results in significantly lower classification
184 errors (maximum 21%) than updated variogram model, especially for the high error values (Fig. 8b),
185 illustrating that the classification error is very much sensitive to the variography model.

186 3.3. Kriging uncertainty

187 For test site T1, the average of standard deviations of ^{137}Cs values simulated at the validation points
188 increases proportional to flight-line spacing. Using all flight-lines (0.9 km flight-line spacing), standard
189 deviation of simulated values is about 12% of the estimation, and using one line out of five (2.5 km
190 flight-line spacing), standard deviation of simulated values reaches 40% of estimation (Fig. 9). For a

contamination threshold of 732 kBq.m^{-2} (P75 of test site T1), the standard deviation of the misclassified area computed based on simulation corresponds to 7% of the estimated misclassified area using all flight-lines and 17% of the estimated value when one line out of five are considered (Fig. 9).

4. Discussion

The analysis of punctual error shows that, in general, adding one kilometer to the flight-line spacing results in 4% increase in the mean difference between measured and estimated ^{137}Cs ground activity at a given point. This increase in punctual error appears to be mainly controlled by the neighboring data configuration of kriging estimators and less sensitive to the variogram model. The relationship between punctual error and flight-line spacing can thus expected to be robust, as supported by similar results obtained in test sites T1 to T5. However, the increase in punctual error is significantly more marked for test site T6. A deeper analysis of the airborne #8 data set over the whole area of interest highlighted that the statistical distribution of ^{137}Cs shows a peak at 6885 Bq.m^{-2}. This could be assimilated to a detection limit. In the test site T6, 17% of the data are set to this value, while less than 2% of the data in the other test sites (Table 2). Uneven presence of fixed values at detection limit (6885 Bq.m^{-2}), decreases predictability of ground activity, which explains high punctual error of T6 (Figure 5).

The analysis of classification error shows that adding one kilometer to the flight-line spacing results in 5% mean increase in the proportion of misclassified contaminated areas (false positive or false negative). This increase in classification error is clearly influenced from the variogram model, thus could be strongly linked to the spatial structure of the ^{137}Cs ground activity: in particular, when distance of spatial correlation (i.e., variogram range) of the ground activity is short, its identification requires a dense flight-line pattern, whereas for contamination with farther distance of spatial correlation flight-line density might be less dense. The experimental semi-variograms computed orthogonal to the flight-lines shows that distance of spatial correlation of activity is the minimum for

test site T2 and the maximum for test site, which thus explains the most (T2) and the least (T3) classification errors. Overall, by increasing flight-line spacing, complexities and detailed variations of contamination structure disappear, and the geometric anisotropy, i.e., directivity, of contamination seems to lose its original form (Fig. 10), especially when focusing on high contamination threshold (i.e., small areas with high activity values).

Analyzing realizations generated by turning bands simulation revealed that the kriging uncertainty also increases with the increase of flight-line spacing: adding one kilometer to the flight-line spacing increases the standard deviation of a punctual estimation by about 6%; and increases the standard deviation of the misclassified area by about 3%. The order of magnitude of the increase of kriging uncertainty is thus similar to that of punctual and classification errors.

Based on the regression error models established in Figs. 5 and 7, the punctual and classification errors for each test site are calculated for the other airborne campaigns (Table 5). For the entire test sites, the errors associated to the latest airborne campaign are about half of those calculated in the earliest campaign, i.e., airborne #4. Otherwise, monitoring and contamination characterization is more accurate in newer airborne campaigns which have denser flight-lines. Since the cost of input data, here flight-line spacing, should be designed according to the value of produced map (Desnoyers and Dubot 2014a, b); such error models could be used in the financial feasibility studies in order to find the optimum flight-line spacing regarding flight cost, decontamination cost and environmental cost from one side, and the goal and value of final contamination map from the other side. As an example, the same flight-line spacing results in more accurate inventory estimation than zonation of polluted soil for decontamination planning. The reason is that the false positive and false negative errors neutralize each other in inventory estimation, however each of them participate in increasing zonation error.

5. Conclusion

The advantages of geophysical airborne data, i.e., good coverage, regular data coordination, rapid acquisition and repeatability, make airborne surveys effective in contamination characterization over a large area. The quality of contamination map produced from the airborne data is yet according to flight-induced parameters such as the FOV or the flight-line spacing.

In this study, the relation between flight-line spacing and two characterization errors (punctual groundsurface activity and contaminated area according to ^{137}Cs threshold) is quantified in six different test sites within the contaminated Fukushima region. Both the errors are positively correlated with the flight-line spacing. In general, adding one kilometer to the flight-line spacing results in: (i) 4% increase in the mean difference between measured and estimated groundsurface activity at a given point; and (ii) 5% increase in the proportion of misclassified contaminated areas (false positive or false negative). These two errors measure different aspects of contamination. The punctual error measures the error on point estimation of groundsurface activity, while the classification error measures the error on zonation for a given threshold. The former appears to be mainly sensitive to the configuration and density of neighboring data, whereas the latter is clearly influenced from the variography analysis. Therefore the accuracy of variography is less important in point groundsurface activity estimation while it is a crucial controlling factor in zonation of contaminated area. In addition, it seems the punctual estimations are more impacted from the increase of flight-line spacing, when the proportion of values below the detection limit in the initial dataset is large.

Practically, for punctual estimation, the accuracy of measurements is probably more crucial than flight-line spacing. On the other hand, for surface characterization, the flight-line spacing needs to be decided relative to the spatial structure of contamination. The order of magnitude of the increase of error was shown to be similar to that of the increase of uncertainty ranges related to punctual value and misclassified; it can thus be informative to compute these ranges, e.g., based on a simulation

approach. Then, the issue of the optimal density of flight-lines can be tackled by asking the question: does the uncertainty range is sufficient for characterizing the variable under study?

For overcoming limitations resulting from a scarce flight-line spacing, a relevant solution would thus consist of integrating the airborne data with other available datasets that are more precise in order to benefit from the positive aspects of multiple datasets, e.g., precision of soil data, abundance of carborne data and good regular coverage of airborne data, e.g., using Bayes' rule (Wainwright et al. 2017, 2018) or co-kriging algorithm.

Acknowledgements and disclaim

The study has been conducted in the context of the TERRITORIES project, and has received funding from the Euratom research and training program 2014-2018 in the framework of the CONCERT [grant agreement No 662287]. Japan Atomic Energy Agency (JAEA) is acknowledged for providing Fukushima airborne datasets accessible for the public and permitting publication of scientific results. Finally, the authors would like to thank Bruno Cessac, Christelle Courbet, Erwan Manach and Christophe Debayle for the scientific and technical exchanges.

This publication reflects only the author's view. Responsibility for the information and views expressed therein lies entirely with the authors. The European Commission is not responsible for any use that may be made of the information it contains.

References

Airo, M.L., Hautaniemi, H., Ville Korhonen, J., Kurimo, M., Levaniemi, H., 2011. Airborne geophysical data management and interpretation. Special Paper - Geological Survey of Finland 49, 349-358.

Bleines, C., Perseval, S., Rambert, F., Renard, D., Touffait, Y., 2004. ISATIS Software Manual, Reference Guide, 5th edn. Geovariances & Ecole des Mines de Paris.

286 Chiles, J.P., Delfiner, P., 2012. Geostatistics, modeling spatial uncertainty, 2nd edn. A John Wiley &
287 Sons, Inc., Hoboken, New Jersey.

288 Desnoyers, Y., Dubot, D., 2014a. Importance des données pour les cartographies géostatistiques de
289 contaminations radiologiques. Spectra Analyse 296, 44-48.

290 Desnoyers, Y., Dubot, D., 2014b. Characterization of radioactive contamination using geostatistics.
291 Nuclear Engineering International 59, 16-18.

292 Gonze, M.A., Renaud, P., Korsakissok, I., Kato, H., Hinton, T.G., Mourlon, C., Simon-Cornu, M., 2014.
293 Assessment of dry and wet atmospheric deposits of radioactive aerosols: Application to Fukushima
294 radiocaesium fallout. Environ. Sci. Technol. 48, 11268–11276. doi: 10.1021/es502590s

295 IAEA, 2003. Guidelines for radioelement mapping using gamma ray spectrometry data. IAEA-
296 TECDOC-1363, IAEA, Vienna.

297 Japan At. Energy Agency (JAEA), 2014. Database for radioactive substance monitoring data [WWW
298 Document]. URL https://emdb.jaea.go.jp/emdb (accessed 2.12.19).

299 Japan Aerosp. eXplor. Agency (JAXA), 2018. High-resolution land use and land cover map products
300 (©JAXA) [WWW Document]. URL https://www.eorc.jaxa.jp/ALOS/en/lulc/lulc_index.htm (accessed
301 2.12.19).

302 Journel, A., Kyriakidis, P.C., Mao, S., 2000. Correcting the Smoothing Effect of Estimators: A Spectral
303 Postprocessor. Math. Geol. 32(7), 787-813. Doi: 10.1023/A:1007544406740

304 Kass, A., 2013. Consequences of flight height and line spacing on airborne (helicopter) gravity
305 gradient resolution in the Great Sand Dunes National Park and Preserve, Colorado. The Leading Edge
306 32, 932-938. doi: 10.1190/tle32080932.1

307 Le Coz, M., Masoudi, P., Cazala, C., 2019. Saptio-temporal variation in cesium-137 ground activity,
308 two years following Fukushima nuclear accident. Manuscript submitted for publication.

309 Lyons, C., Colton, D., 2012 Aerial measuring system in Japan. Health Phys. 102, 509-515. doi:
310 10.1097/HP.0b013e31824d0056

311 Malins, A., Okumura, M., Machida, M., Takemiya, H., Saito, K., 2015. Fields of view for environmental
312 radioactivity. In: Proceedings of the international symposium on radiological issues for Fukushima's
313 revitalized future, pp 28-34.

314 Masoudi, P., Le Coz, M., Cazala, C., Saito, K., 2019. Spatial properties of soil analyses and airborne
315 measurements for reconnaissance of soil contamination by ^{137}Cs after Fukushima nuclear accident in
316 2011. J. Environ. Radioact. 202, 74-84. doi: 10.1016/j.jenvrad.2018.11.014

317 Minty, B.R.S., 1997. Fundamentals of airborne gamma-ray spectrometry. AGSO Journal of Australian
318 Geology and Geophysics 17, 39-50.

319 Rabus, B., Eineder, M., Roth, A., Bamler, R., 2003. The shuttle radar topography mission (SRTM) - A
320 new class of digital elevation models acquired by spaceborne radar. ISPRS J. Photogramm. Remote
321 Sens. 57, 241-262. doi:10.1016/S0924-2716(02)00124-7

322 Reeves, C., 2005. Aeromagnetic Surveys: Principles, Practice and Interpretation. Earth-works,
323 Washington DC.

324 Saito, K., Onda, Y., 2015. Outline of the national mapping projects implemented after the Fukushima
325 accident. J. Environ. Radioact. 139, 240-249. doi: 10.1016/j.jenvrad.2014.10.009

326 Sanada, Y., Sugita, T., Nishizawa, Y., Kondo, A., To, T., 2014. The aerial radiation monitoring in Japan
327 after the Fukushima Daiichi nuclear power plant accident. Progress in Nuclear Science and
328 Technology 4, 76-80. doi: 10.15669/pnst.4.76

329 Sanderson, D.C.W., Cresswell, A.J., White, D.C., 2008. The effect of flight line spacing on radioactivity
330 inventory and spatial feature characteristics of airborne gamma-ray spectrometry data. Int. J.
331 Remote Sens. 29, 31-46. doi: 10.1080/01431160701268970

Sanderson, D.C.W., Cresswell, A.J., White, D.C., Murphy, S., McLeod, J., 2001. Investigation of Spatial and Temporal Aspects of Airborne Gamma Spectrometry. Project Report, Department of the Environment, Transport and the Regions, East Kilbride.

Wackernagel, H., 2003. Multivariate geostatistics: an introduction with applications, 3rd edn. Springer-Verlag Berlin Heidelberg GmbH, Heidelberg.

Wainwright, H.M., Seki, A., Chen, J., Saito, K., 2017. A multiscale Bayesian data integration approach for mapping air dose rates around the Fukushima Daiichi Nuclear Power Plant. J. Environ. Radioact. 167, 62-69. doi: 10.1016/j.jenvrad.2016.11.033

Wainwright, H.M., Seki, A., Mikami, S., Saito, K., 2018. Characterizing regional-scale temporal evolution of air dose rates after the Fukushima Daiichi Nuclear Power Plant accident. J. Environ. Radioact. 189, 213-220. doi: 10.1016/j.jenvrad.2018.04.006

Tables

Table 1. Specifications of the airborne survey datasets #3 to #8 available from the MEXT in the Fukushima region.

Airborne	#3	#4	#5	#6	#7	#8
Start date	04.06.2011	25.10.2011	22.06.2012	31.03.2012	27.08.2013	05.11.2013
End date	02.07.2011	05.11.2011	28.06.2012	15.11.2012	18.09.2013	18.11.2013
Base date	02.07.2011	05.11.2011	28.06.2012	16.11.2012	28.09.2013	19.11.2013
^{137}Cs mean (kBq/m^2)	402	193	313	230	310	280
Flight-line spacing (m)	1.8-2 km	1.8-2 km	1.8 km	1.8 km	0.6-0.9 km	0.6-0.9 km

Table 2. Specifications of each test site selected for the study.

	T1	T2	T3	T4	T5	T6
Flight-line spacing (m)	920	920	840	960	610	920
Mean survey	356	368	355	362	356	369

altitude (m agl)						
Mean distance between measurements along flight-lines (m)	51	43	46	44	51	49
Number of validation data	100	100	100	91	136	92
^{137}Cs distribution	lognormal	semi-gaussian	lognormal	lognormal	lognormal	lognormal
^{137}Cs mean (kBq/m^2)	509	73	122	94	1424	63
^{137}Cs 3rd quartile (P75) (kBq/m^2)	732	93	131	115	1852	42
^{137}Cs = 6885 Bq/m^2 (% of the area)	0	1.9	2.2	0.2	0	17.5

348

349 Table 3. Flight-line selections and the average of the flight-line spacing for test site T1 (see Fig 1b).

350 Selection 1/j-k means one line is selected every j successive lines. k varies from 1 to j, and represents

351 all the possible selections of one line every j lines.

Name	Selected lines			Flight-line spacing (m)
	LW	L	LE	
All the lines	all	all	all	920
Selection 1/2-1	1-2-3-4-5-7-8-9-10-11	2-4-6-8-10	1-2-5-6-9-10-13-14-17-18-21	1270
Selection 1/2-2	2-3-4-5-6-9-10-11	1-5-7-9-11	3-4-7-8-11-12-15-16-19-20	1270
Selection 1/3-1	1	2-3-4-5-6-7-8-9-10-11	1	1840
Selection 1/3-2	3-4-5-6-7-8-9-10-11	1	4-6-8-10-12-14-16-18-20	2030
Selection 1/3-3	2-4-5-7-8-9-10-11	-	2-5-7-9-11-13-15-17-19-21	2030
Selection 1/4-1	1-3-7-8-11	5-9	1-4-7-12-15-20	2530
Selection 1/4-2	3-6-7-10-11	3-4-8	10-13-18-21	2530
Selection 1/4-3	2-5-8-9	3-6	2-5-8-14-17-20	2890
Selection 1/4-4	4-7-8-11	2-5-9	7-12-15-20	2890
Selection 1/5-1	1-3-5-8-10	6-11	1-5-8-15-18	2890
Selection 1/5-2	5-7-10	1-3-8	9-12-19	3380

Selection 1/5-3	2-4-7-9	5-10	2-6-13-16	3380
Selection 1/5-4	2-4-6-11	7-9	3-7-10-17-20	3380
Selection 1/5-5	6-8-11	2-4-9	11-14-21	3380
Selection 1/6-1	1	3-5-7-9-11	1	3380
Selection 1/6-2	4-6-8-10	1	6-10-14-18	4050
Selection 1/6-3	2-4-6-8-10	-	2-7-11-15-19	4050
Selection 1/6-4	2	4-6-8-10	3	4050
Selection 1/6-5	5-7-9-11	2	12-16-20	4050
Selection 1/6-6	3-5-7-9-11	-	4-9-13-17-21	4050
Selection 1/7-1	1-4-6-11	8	1-6-11-20	4050
Selection 1/7-2	4-9-11	1-6	7-16-21	4050
Selection 1/7-3	2-7-9	4-11	2-12-17	4050
Selection 1/7-4	2-5-7	9	3-8-13	5060
Selection 1/7-5	5-10	2-7	9-18	5060
Selection 1/7-6	3-8-10	5	4-14-19	5060
Selection 1/7-7	3-6-8	10	5-10-15	5060

352

353 Table 4. Specification of interpolation procedure in each test site.

		T1	T2	T3	T4	T5	T6
Data preparation	Logarithmic transformation (cf. stage i, Fig.2)	✓	✓	×	×	×	×
	Deterministic model (cf. stage ii-ii, Fig. 2)	✓ (Average 10km)	✓ (Average 5km)	×	×	×	×
Results	Zonal anisotropy (according to variography, stage iv, Fig. 2)	✓	×	✓ (Strongly)	✓	✓ (Strongly)	✓
	Geometric anisotropy	135°	45°	115°	22° (Slightly)	135°	110°

354

355 Table 5. Generalization of the errors calculated from campaign airborne #8 to airborne campaigns #3

356 to #7.

Test site	Airborne	Base date	Flight-line spacing [km]	Punctual error	Classification error
T1	#3	02.07.2011	1.8	8%	10%
	#4	05.11.2011	1.8	8%	10%

	#5	28.06.2012	1.8	8%	10%
	#6	16.11.2012	1.8	8%	10%
	#7	28.09.2013	0.6	3%	4%
	#8	19.11.2013	0.6	3%	4%
T2	#3	02.07.2011	2	9%	19%
	#4	05.11.2011	2	9%	19%
	#5	28.06.2012	1.8	8%	17%
	#6	16.11.2012	1.8	8%	17%
	#7	28.09.2013	0.9	5%	9%
	#8	19.11.2013	0.9	5%	9%
T3	#3	02.07.2011	2	9%	6%
	#4	05.11.2011	2	9%	6%
	#5	28.06.2012	1.8	8%	5%
	#6	16.11.2012	1.8	8%	5%
	#7	28.09.2013	0.9	5%	3%
	#8	19.11.2013	0.9	5%	3%
T4	#3	02.07.2011	2	9%	11%
	#4	05.11.2011	2	9%	11%
	#5	28.06.2012	1.8	8%	10%
	#6	16.11.2012	1.8	8%	10%
	#7	28.09.2013	0.9	5%	6%
	#8	19.11.2013	0.9	5%	6%
T5	#3	02.07.2011	1.8	8%	10%
	#4	05.11.2011	1.8	8%	10%
	#5	28.06.2012	1.8	8%	10%
	#6	16.11.2012	1.8	8%	10%
	#7	28.09.2013	0.6	3%	4%
	#8	19.11.2013	0.6	3%	4%
T6	#3	02.07.2011	1.8	13%	10%
	#4	05.11.2011	1.8	13%	10%
	#5	28.06.2012	1.8	13%	10%
	#6	16.11.2012	1.8	13%	10%
	#7	28.09.2013	0.9	6%	6%
	#8	19.11.2013	0.9	6%	6%

Figure captions

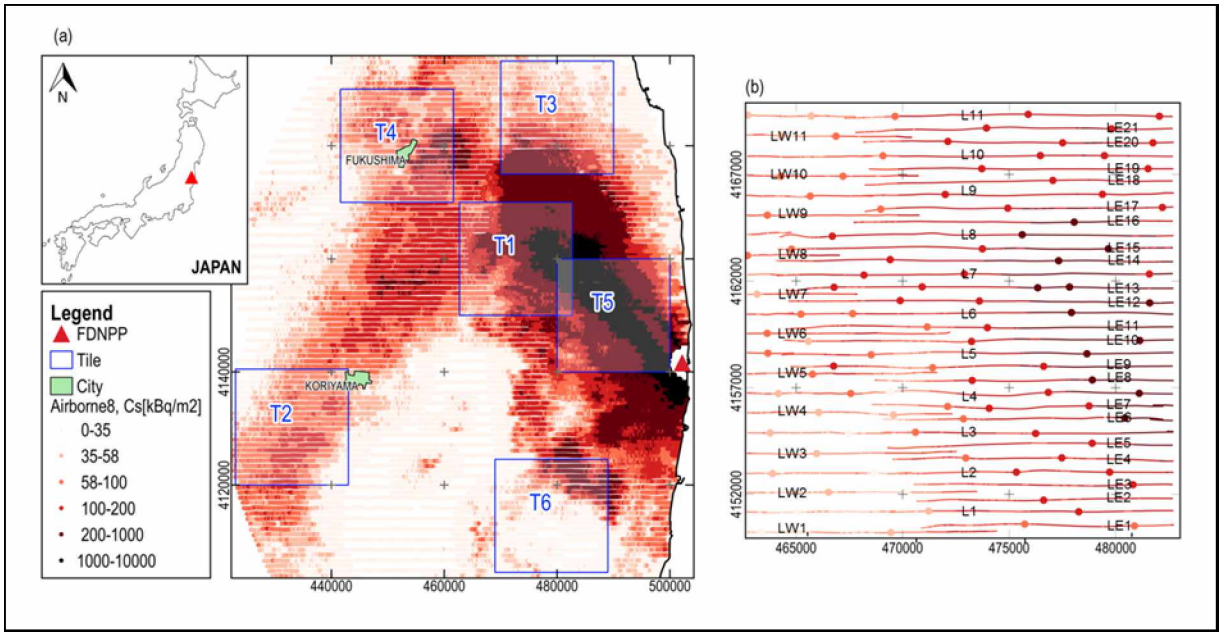

359

360 Fig. 1. Location of six test sites selected in this study (a). Location of flight-lines of airborne #8 inside
361 test site T1 (b). The validation data are bolded. L: a complete flight-line, LE (LW): an incomplete flight-
362 line, which extends to the Eastern (Western) border of the test site.

363

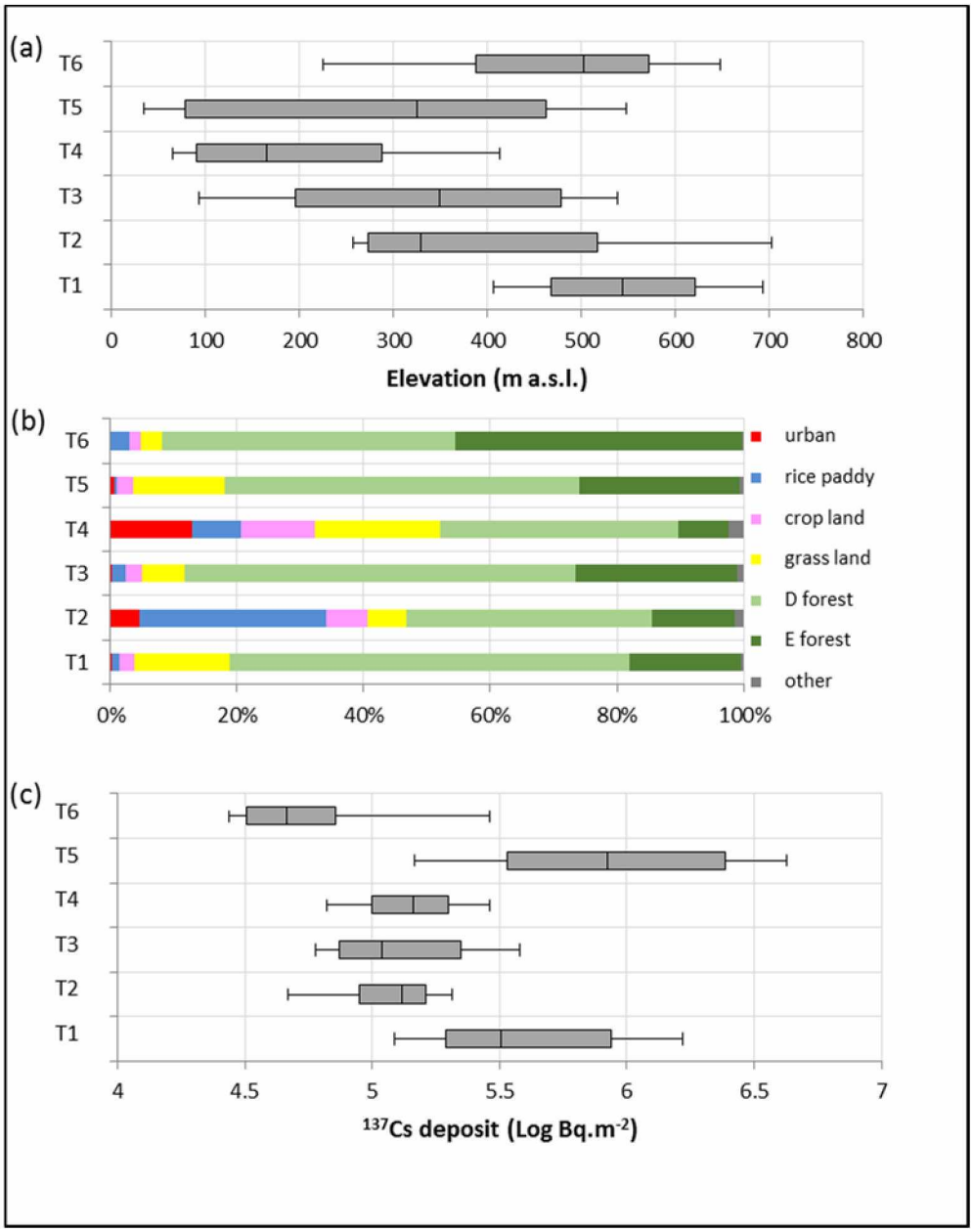

364

365 Fig. 2. Distribution of SRTM DEM elevation (Rabus et al., 2003) (a), land cover types (JAXA , 2018) (b)

366 and ^{137}Cs ground deposit from airborne #8 dataset (c) for test sites T1 to T6.

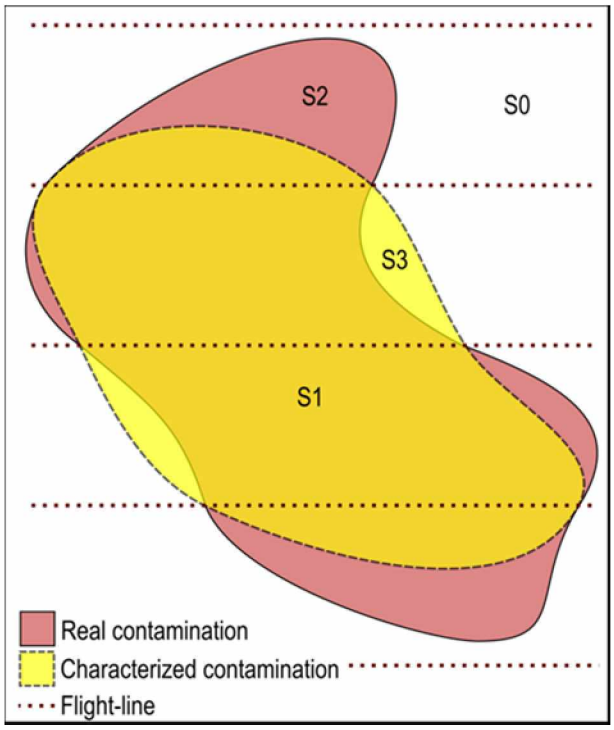

Fig. 3. Schematic partitioning of whole the study area according to the “considered as” real and characterized contaminated areas: S0 and S1 are correctly characterized surfaces while S2 and S3 are false negative and false positive characterized surfaces, respectively.

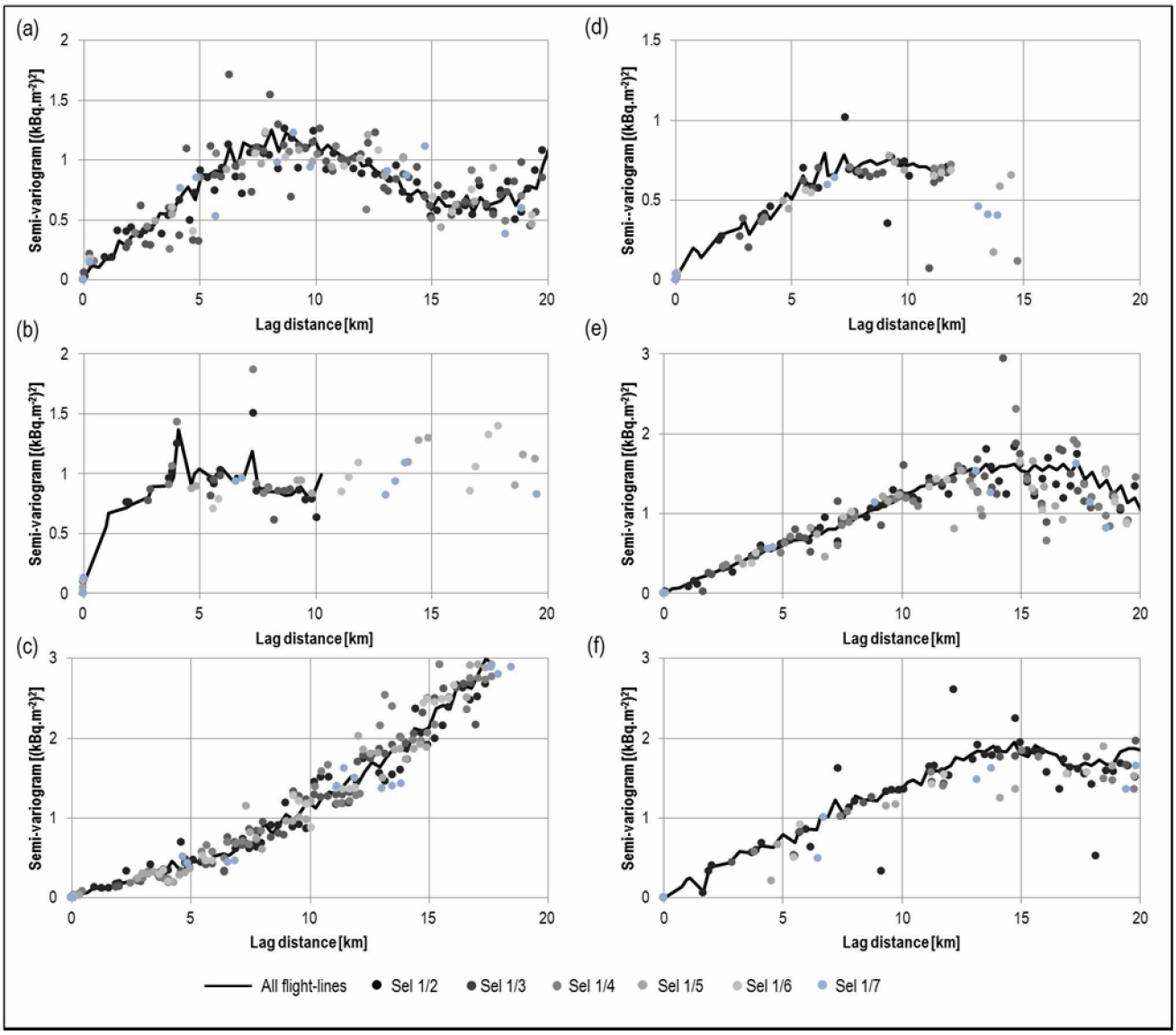

371

372 Fig. 4. Experimental semi-variogram computed orthogonal to the flight-lines for test sites T1 to T6 (a

373 to f) with various flight-line selections.

374

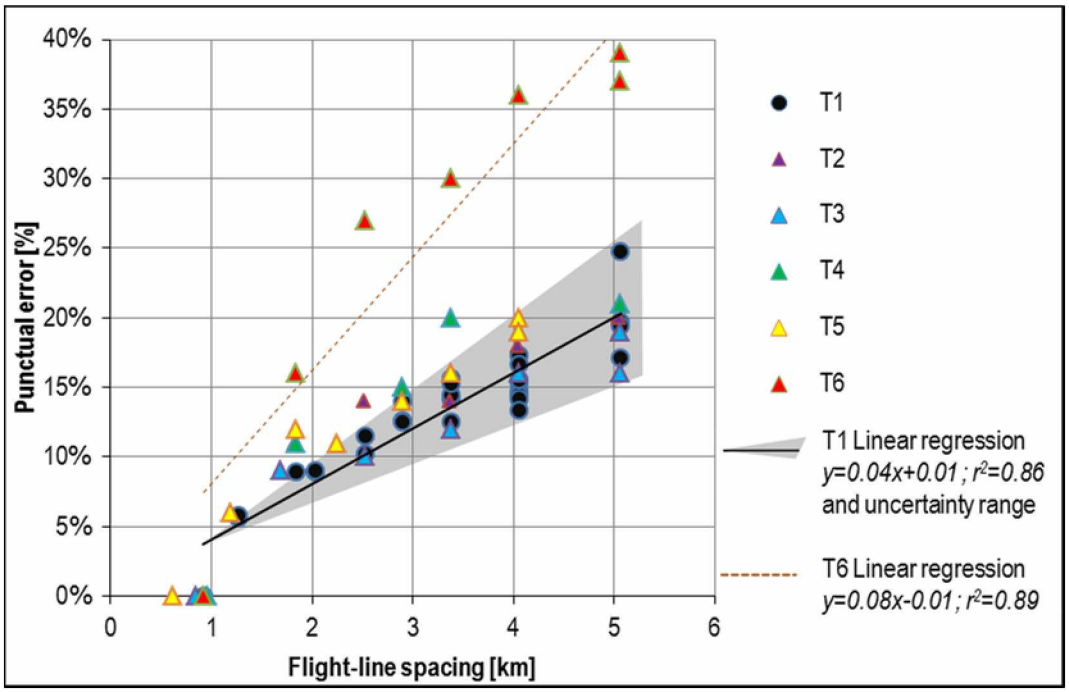

375

376 Fig. 5. The punctual error of validation data versus flight-line spacing, following applying point

377 ordinary kriging.

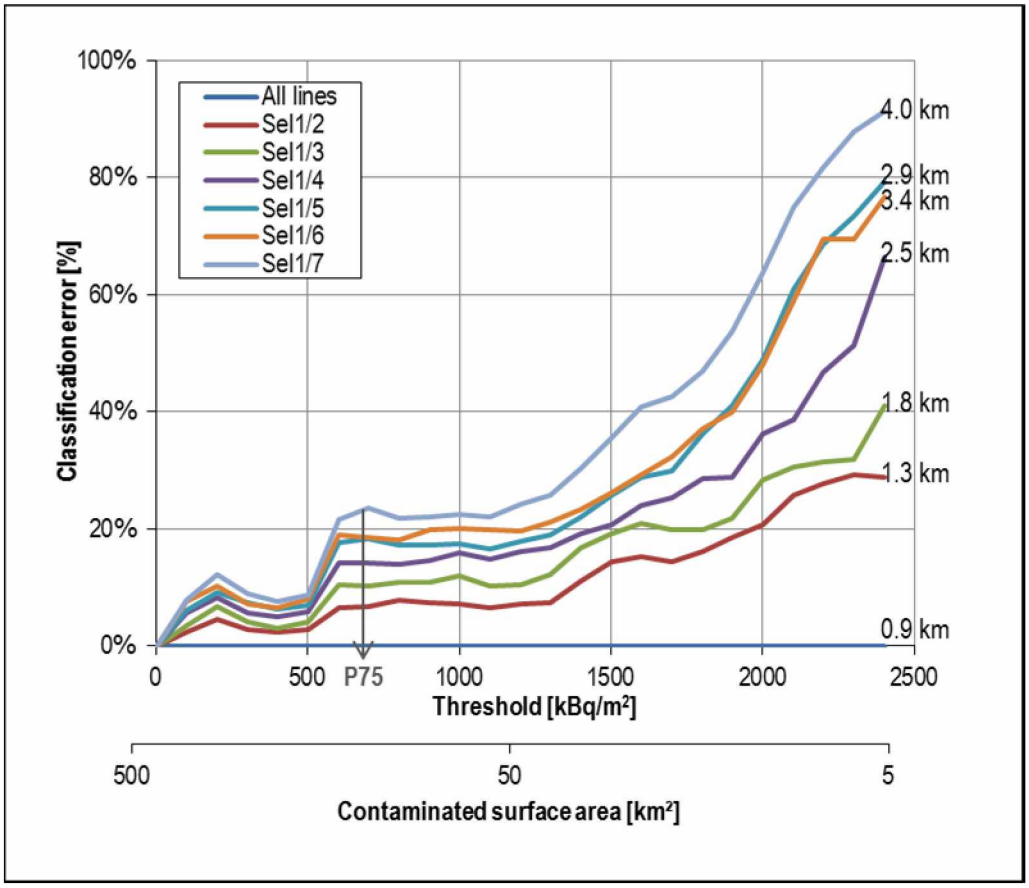

378

379 Fig. 6. The classification error versus threshold and corresponding contaminated surface area, test
380 site T1.

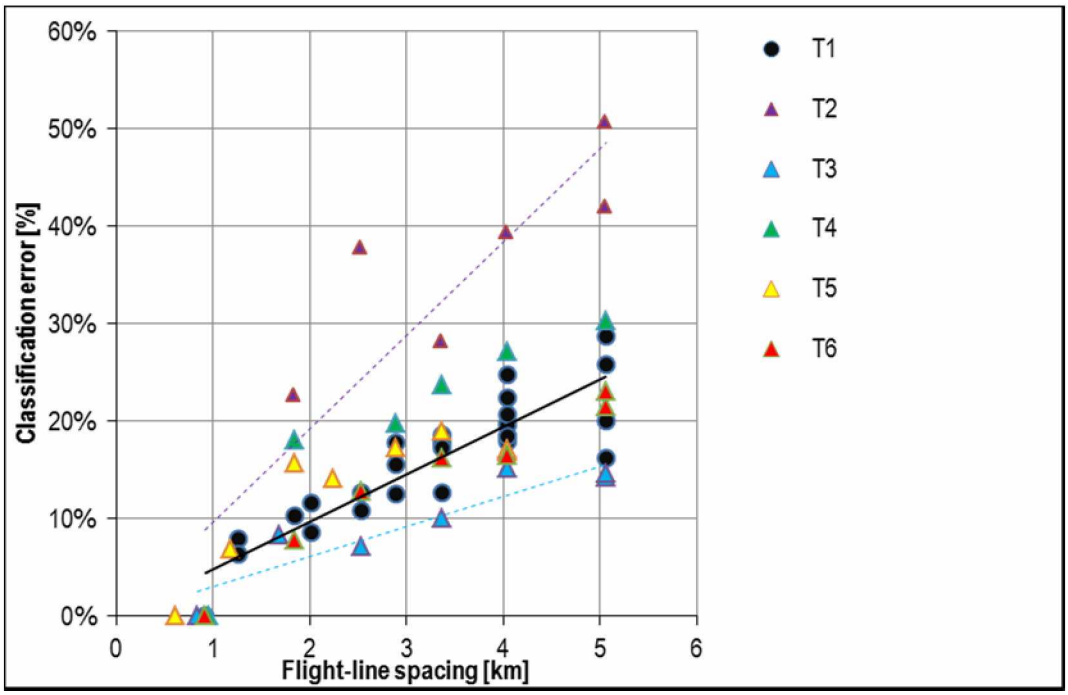

381

382 Fig. 7. The classification error versus flight-line spacing, following applying block ordinary kriging. The
383 threshold is always P75 (Table 2).

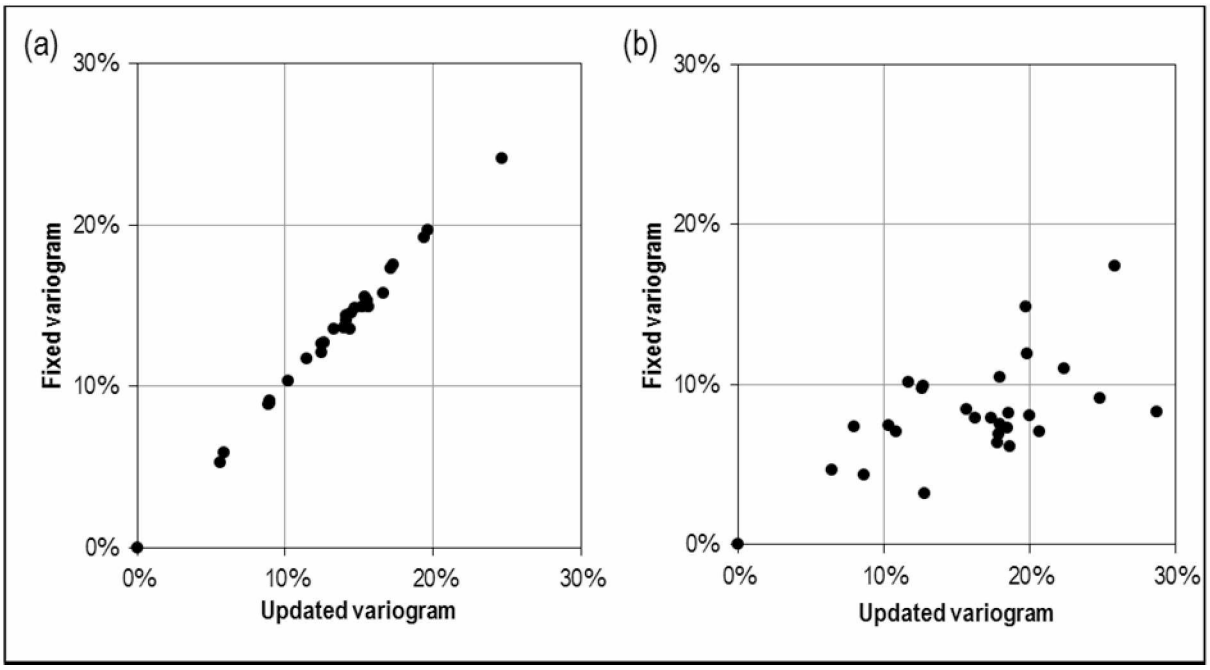

384

385 Fig. 8. Sensitivity of punctual (a) and classification (b) errors according to subjective variography
386 analysis, in test site T1.

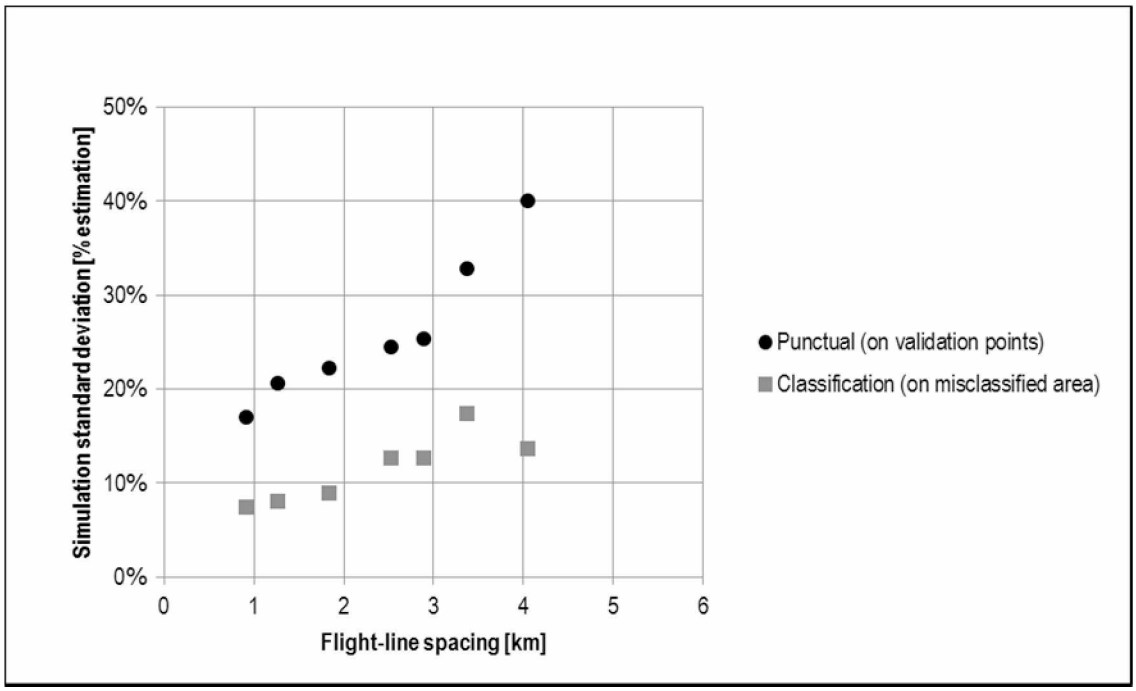

387

388 Fig. 9. Standard deviations of the ^{137}Cs values simulated at validation points and of the simulated
389 misclassified areas for test site T1.

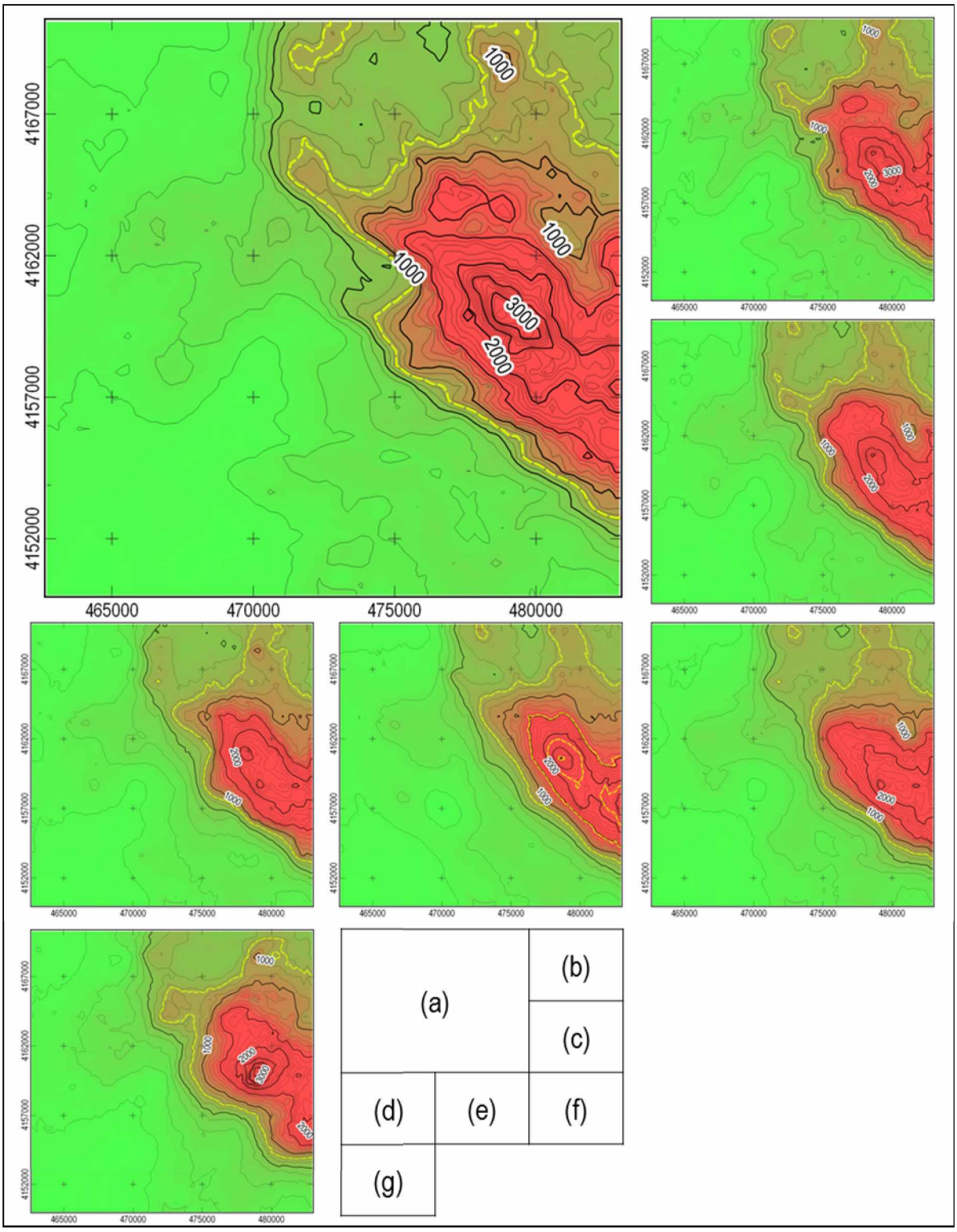

390

391 Fig. 10. Contamination map of ^{137}Cs, estimated by block kriging at the grids of 250 m × 250 m in test
392 site T1, using all flight-lines (a), selection 1/2-1 (b), selection 1/3-1 (c), selection 1/4-1 (d), selection
393 1/5-1 (e), selection 1/6-1 (f) and selection 1/7-1 (g). The contour values are in [kBq/m2]. Dashed-line
394 is contamination threshold, i.e. 732 $kBq.m^{-2}$ (Table 2).